

# Linear Free Energy Relationships between Dissolution Rates and Molecular Modeling Energies of Rhombohedral Carbonates

Owen W. Duckworth,<sup>†,§</sup> Randall T. Cygan,<sup>‡</sup> and Scot T. Martin<sup>\*,†</sup>

Division of Engineering and Applied Sciences, Pierce Hall, 29 Oxford Street,  
Harvard University, Cambridge, Massachusetts 02138, and Geochemistry Department,  
Sandia National Laboratories, Albuquerque, New Mexico 87185-0750

Received July 24, 2003. In Final Form: December 18, 2003

Bulk and surface energies are calculated for endmembers of the isostructural rhombohedral carbonate mineral family, including Ca, Cd, Co, Fe, Mg, Mn, Ni, and Zn compositions. The calculations for the bulk agree with the densities, bond distances, bond angles, and lattice enthalpies reported in the literature. The calculated energies also correlate with measured dissolution rates: the lattice energies show a log-linear relationship to the macroscopic dissolution rates at circumneutral pH. Moreover, the energies of ion pairs translated along surface steps are calculated and found to predict experimentally observed microscopic step retreat velocities. Finally, pit formation excess energies decrease with increasing pit size, which is consistent with the nonlinear dissolution kinetics hypothesized for the initial stages of pit formation.

## 1. Introduction

The rhombohedral carbonate mineral family comprises 4% of the earth's crust,<sup>1</sup> and the precipitation and dissolution cycles of carbonates have significant environmental impacts. Within the family, calcium and magnesium carbonates are the most abundant. They influence the chemistry of the ocean and the global cycling of carbon.<sup>2,3</sup> They also alter pH and alkalinity in local terrestrial environments<sup>4</sup> and thus partially regulate the fate and transport of anthropogenic pollutants, especially heavy metals.<sup>5–12</sup> Furthermore, precipitation and dissolution of other rhombohedral carbonate minerals, which include the Cd, Co, Fe, Mn, Ni, and Zn endmembers, directly affect the cycling of these micronutrient and contaminant metals.<sup>5,13–20</sup> A detailed understanding of

the processes of precipitation and dissolution is essential for a quantitative predictive capability for carbonate dissolution.

State-of-the-art microscopic observations of carbonate dissolution are provided in Figure 1. A time series of atomic force micrographs shows the expansion of crystallographically controlled pits bound by [441] and [481] steps on the (1014) surface of calcite. The (1014) surface of the rhombohedral carbonate mineral family dissolves by pit formation and subsequent expansion of the pit by step retreat.<sup>21–26</sup> Step retreat is a complex multicomponent molecular mechanism, for which the individual chemical reactions are difficult to observe experimentally.

Molecular simulations are a promising complementary approach for investigating the separate components of the dissolution mechanism. Molecular models can predict processes at scales different from observations and provide cohesive insightful explanations at scales equal to observations. For these applications, model accuracy is key. A renewed basis for the development of accurate models of energetics and kinetics of surface microtopography, including pits, steps, and kinks, is offered by the new observations of modern microscopic and spectroscopic techniques.<sup>24,25,27–29</sup>

\* To whom correspondence should be addressed. E-mail: smartin@deas.harvard.edu.

<sup>†</sup> Harvard University.

<sup>‡</sup> Sandia National Laboratories.

<sup>§</sup> Present address: Department of Civil and Environmental Engineering, University of California, Berkeley, CA 94720.

(1) Raymond, L. A. *Petrology: The Study of Igneous, Sedimentary, and Metamorphic Rocks*; Wm. C. Brown: Dubuque, IA, 1995.

(2) Pilson, M. E. Q. *An Introduction to the Chemistry of the Sea*; Prentice Hall: Upper Saddle River, NJ, 1998.

(3) Schlesinger, W. H. *Biogeochemistry: An Analysis of Global Change*, 2nd ed.; Academic Press: San Diego, 1997.

(4) Stumm, W.; Morgan, J. J. *Aquatic Chemistry*, 3rd ed.; Wiley: New York, 1996.

(5) Amirbahman, A.; Schoenberger, R.; Johnson, C. A.; Sigg, L. *Environ. Sci. Technol.* **1998**, *32*, 1933.

(6) Stipp, S. L. S.; Konnerup-Madsen, J.; Franzreb, K.; Kulik, A.; Mathieu, H. *Nature* **1998**, *396*, 356.

(7) Hoffman, U.; Stipp, S. L. S. *Geochim. Cosmochim. Acta* **2001**, *65*, 4131.

(8) Warren, L. A.; Maurice, P. A.; Parmar, N.; Ferris, F. G. *Geomicrobiol. J.* **2001**, *18*, 93.

(9) Reeder, R. J.; Nugent, M.; Tait, C. D.; Morris, D. E.; Heald, S. M.; Beck, K. M.; Hess, W. P.; Lazirotti, A. *Geochim. Cosmochim. Acta* **2001**, *65*, 3491.

(10) Reeder, R. J. *Geochim. Cosmochim. Acta* **1996**, *60*, 1543.

(11) Elzinga, E. J.; Reeder, R. J. *Geochim. Cosmochim. Acta* **2002**, *66*, 3943.

(12) Elzinga, E. J.; Reeder, R. J.; Withers, S. H.; Peale, R. E.; Mason, R. A.; Beck, K. M.; Hess, W. P. *Geochim. Cosmochim. Acta* **2002**, *66*, 2875.

(13) Erly, L. E. *Appl. Geochem.* **1999**, *14*, 963.

(14) Garralon, A.; Gomez, P.; Turrero, M. J.; Sanchez, M.; Melon, A. *M. Sci. Total Environ.* **1999**, *242*, 27.

(15) Li, Y. H.; Bischoff, J.; Mathieu, G. *Earth Planet. Sci. Lett.* **1969**, *7*, 265.

(16) Calvert, S. E.; Price, N. B. *Earth Planet. Sci. Lett.* **1972**, *16*, 245.

(17) Middelburg, J. J.; De Lange, G. L.; Van Der Weijden, C. H. *Geochim. Cosmochim. Acta* **1987**, *51*, 759.

(18) Jensen, D. L.; Boddum, J. K.; Tjell, J. C.; Christensen, T. H. *Appl. Geochem.* **2002**, *17*, 503.

(19) Wersin, P.; Charlet, L.; Karthein, R.; Stumm, W. *Geochim. Cosmochim. Acta* **1989**, *53*, 2787.

(20) Morgan, J. J. Chemical equilibria and kinetic properties of manganese in natural water. In *Principles and Applications of Water Chemistry*; Faust, S., Hunter, J., Eds.; Wiley: New York, 1967; p 561.

(21) Hillner, P. E.; Gratz, A. J.; Manne, S.; Hansma, P. K. *Geology* **1992**, *20*, 359.

(22) Liang, Y.; Baer, D. R.; McCoy, J. M.; Amonette, J. E.; LaFemina, J. P. *Geochim. Cosmochim. Acta* **1996**, *60*, 4883.

(23) Duckworth, O. W.; Martin, S. T. *Am. Mineral.*, in press.

(24) Duckworth, O. W.; Martin, S. T. *Geochim. Cosmochim. Acta* **2004**, *68*, 607.

(25) Duckworth, O. W.; Martin, S. T. *Geochim. Cosmochim. Acta* **2003**, *67*, 1787.

(26) Jordan, G.; Higgins, S. R.; Eggleston, C. M.; Knauss, K. G.; Schmah, W. W. *Geochim. Cosmochim. Acta* **2001**, *65*, 4257.

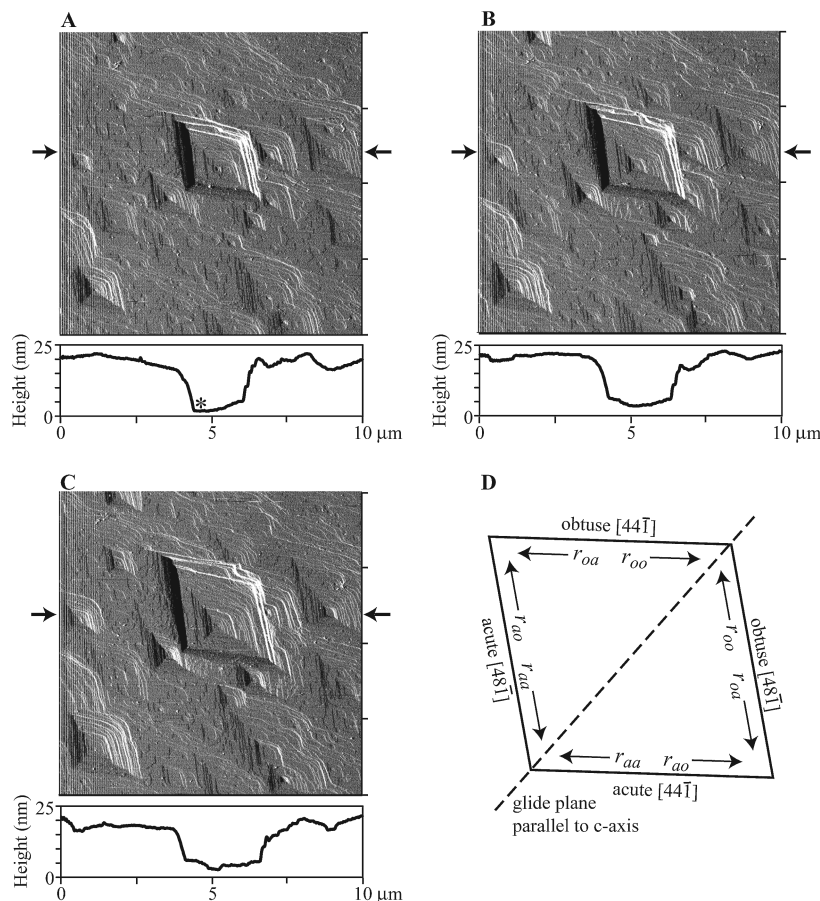


**Figure 1.** (A–C) Time series of atomic force micrographs of the  $(10\bar{1}4)$  surface of calcite. Micrographs are collected in contact mode in aqueous fluid with silicon nitride probes at a scanning rate of 4 Hz. Images are presented in deflection mode, while the associated cross-sections are from height data. Arrows indicate the start and end points of the cross-sections. Further detail on experimental methodology is reported in ref 25. The aqueous solution has pH = 8.8. The time between images is 4.25 min. (D) Schematic diagram of the step orientation and ion pair translation direction in pits. (The asterisk at the bottom of the pit cross-section in panel A is discussed in the caption of Figure 6.)

The hypothesis tested in our current study is that linear free energy relationships (LFERs) exist between calculated energies and observed dissolution rates. Our approach is to calculate the energies of the rhombohedral carbonates by molecular mechanics methods using a rigid ion model and then to test correlations between these energies (including lattice energies, pit formation excess energies, and ion pair translation energies) and known dissolution rates.<sup>23–25,30</sup>

## 2. Approach

**2.1. Theory.** The potential energies of bulk and surface structures are calculated by a rigid ion model. Classical physical forces act upon an interconnected locus of atoms. Previous implementations include investigations of defects,<sup>31–33</sup> growth,<sup>34–39</sup> dissolution,<sup>40</sup> sorption,<sup>39,41</sup> and

solvation<sup>37,42,43</sup> of carbonate minerals. The present approach is based on the Born model of solids, where ions interact by electrostatic and short-range forces. The total system energy  $U_T$  ( $\text{kJ mol}^{-1}$ ) includes contributions from the electrostatic energy ( $U_{ij}^e$ ), short-range electronic attraction and repulsion energy ( $U_{ij}^{sr}$ ), and intramolecular energies ( $U_{C-O}^m$ ,  $U_{O-C-O}^b$ ,  $U_{O-C-O-O}^t$ ), as follows:

$$U_T = \sum_i \sum_j U_{ij}^e + \sum_i \sum_j U_{ij}^{sr} + \sum_{\text{CO}_3^{2-}} (U_{C-O}^m + U_{O-C-O}^b + U_{O-C-O-O}^t) \quad (1)$$

where the sums are across  $i$  and  $j$  atoms and all carbonate groups. Short-range interactions are calculated to a spline cutoff of 16.5 Å, while electrostatic calculations are

(27) Duckworth, O. W.; Martin, S. T. *Geochim. Cosmochim. Acta* **2001**, *23*, 4289.

(28) Brown, G. E.; Parks, G. A. *Int. Geol. Rev.* **2001**, *43*, 963.

(29) Hind, A. R.; Bhargava, S. K.; McKinnon, A. *Adv. Colloid Interface Sci.* **2001**, *93*, 91.

(30) Perry, T. D.; Duckworth, O. W.; McNamara, C. J.; Martin, S. T.; Mitchell, R. Submitted.

(31) Cygan, R. T.; Wright, K.; Fislser, D. K.; Gale, J. D.; Slater, B. *Mol. Simul.* **2002**, *28*, 475.

(32) Wright, K.; Cygan, R. T.; Slater, B. *Geochim. Cosmochim. Acta* **2002**, *66*, 2541.

(33) Fislser, D. K.; Gale, J. D.; Cygan, R. T. *Am. Mineral.* **2000**, *85*, 217.

(34) de Leeuw, N. H. *J. Phys. Chem. B* **2002**, *1006*, 5241.

(35) de Leeuw, N. H. *Am. Mineral.* **2002**, *87*, 679.

(36) Braybrook, A. L.; Heywood, B. R.; Jackson, R. A.; Pitt, K. J. *Cryst. Growth* **2002**, *243*, 336.

(37) de Leeuw, N. H.; Parker, S. C. *Phys. Chem. Chem. Phys.* **2001**, *3*, 3217.

(38) Titiloye, J. O.; de Leeuw, N. H.; Parker, S. C. *Geochim. Cosmochim. Acta* **1998**, *62*, 2637.

(39) Ojo, S. A.; Slater, B.; Catlow, C. R. A. *Mol. Simul.* **2002**, *28*, 591.

(40) de Leeuw, N. H.; Parker, S. C.; Harding, J. H. *Phys. Rev. B* **1999**, *60*, 13792.

(41) de Leeuw, N. H.; Parker, S. C. *J. Chem. Phys.* **2000**, *112*, 4326.

(42) Wright, K.; Cygan, R. T.; Slater, B. *Phys. Chem. Chem. Phys.* **2001**, *3*, 839.

(43) Hwang, S.; Blanco, M.; Goddard, W. A. *J. Phys. Chem. B* **2001**, *105*, 10746.

**Table 1. Interaction Parameters<sup>a</sup>**

Coulombic Parameters (Reference 33)			
atom	charge ( <i>e</i> )		
Ca, Cd, Co, Fe, Mg, Mn, Ni, Zn	2.0000		
C	1.3435		
O	-1.1450		
Born-Mayer and van der Waals Potential (References 33 and 36)			
ion pair	<i>D</i> (kJ mol <sup>-1</sup> )	$\beta \times 10^{-10}$ (m <sup>-1</sup> )	$C \times 10^{60}$ (kJ m <sup>6</sup> mol <sup>-1</sup> )
Ca-O	852 875.84	4.199 39	
Cd-O	417 769.52	3.901 68	
Co-O	105 710.91	3.492 84	
Fe-O	207 638.65	3.772 16	
Mg-O	100 306.72	3.456 62	
Mn-O	193 064.31	3.667 03	
Ni-O	157 703.82	3.750 94	
Zn-O	99 322.55	3.459 01	
O-O	3 474 566.97	5.061 75	2107.62
Morse Potential (Reference 47)			
<i>D</i> <sub>O</sub> (kJ mol <sup>-1</sup> )	$\alpha \times 10^{-10}$ (m <sup>-1</sup> )	<i>r</i> <sub>0</sub> × 10 <sup>10</sup> (m)	
C-O	6140.92	2.5228	1.2940
Three-Body Potential (Reference 47)			
<i>k</i> <sub>b</sub> (kJ mol <sup>-1</sup> rad <sup>-2</sup> )		$\theta_0$ (rad)	
O-C-O		2.0944	
Four-Body Potential (Reference 47)			
O-C-O-O			<i>k</i> <sub>t</sub> (kJ mol <sup>-1</sup> )
O-C-O-O			513.80

<sup>a</sup> Symbols are defined in the text.

performed as an Ewald summation, part of which resides in reciprocal space, to minimize computational expense and ensure convergence.<sup>44</sup>

The electrostatic energy between two atoms is Coulombic:

$$U_{ij}^e = \frac{e^2 Z_i Z_j}{4\pi\epsilon_0 r_{ij}} \quad (2)$$

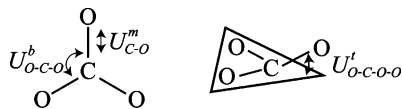
where *e* is the fundamental charge on an electron (C), *Z* is the charge on atom *i* or *j*,  $\epsilon_0$  is vacuum permittivity (C<sup>2</sup> kJ<sup>-1</sup> m<sup>-1</sup>), and *r*<sub>ij</sub> (m) is the distance separating atoms *i* and *j*.

Short-range O-O and M-O interactions are calculated using a Born-Mayer and van der Waals potential:

$$U_{ij}^{sr} = D_{ij} \exp(-\beta_{ij} r_{ij}) - C_{ij} r_{ij}^{-6} \quad (3)$$

where *D*<sub>ij</sub> (kJ mol<sup>-1</sup>),  $\beta_{ij}$  (m<sup>-1</sup>), and *C*<sub>ij</sub> (kJ m<sup>6</sup> mol<sup>-1</sup>) are empirical parameters for short-range interactions (Table 1).

The intramolecular energies within each carbonate unit are the sum of several terms, as illustrated below. A Morse



potential for each C-O bond calculates the energy for changes in bond length from an equilibrium value:

$$U_{C-O}^m = D_0 (\exp(-\alpha(r - r_0)) - 1)^2 \quad (4)$$

where *D*<sub>0</sub> (kJ mol<sup>-1</sup>) is the bond dissociation energy,  $\alpha$  (m<sup>-1</sup>) depends on the vibrational force constant, and *r*<sub>0</sub> (m) is the equilibrium bond distance. A harmonic potential describes the O-C-O bending energy, as follows:

$$U_{C-O-O}^b = 0.5k_b(\theta - \theta_0)^2 \quad (5)$$

where  $\theta_0$  is the equilibrium bond angle (120°) and *k*<sub>b</sub> (kJ mol<sup>-1</sup> rad<sup>-2</sup>) is an empirical force constant. The torsional energy of the dihedral O-C-O-O angle ( $\varphi$ ) arises from out-of-plane distortion of the carbonate group and is calculated as a four-body potential:

$$U_{O-C-O-O}^t = k_t(1 + \cos \varphi) \quad (6)$$

where *k*<sub>t</sub> (kJ mol<sup>-1</sup>) is an empirical force constant. The planar carbonate group has  $\varphi = 180^\circ$ . The angle decreases and the torsional energy increases as an oxygen atom is deflected out of the plane.

For a structure assembled from gas-phase ions (*U* = 0), the energy of the bulk system obtained by eq 1 corresponds to the lattice energy (*U*<sub>L</sub>). Because the calculations are conducted at constant pressure, *U*<sub>L</sub> is equal to lattice enthalpy ( $\Delta H_L$ ).

**2.2. Computational Methodology.** Energy calculations are performed using the molecular simulation tools provided in Cerius<sup>2</sup> (Accelrys, San Diego, CA). The Open Force Field energy module within Cerius<sup>2</sup> minimizes *U*<sub>T</sub> of eq 1 by adjusting the spatial coordinates of M, C, and O atoms under constant pressure conditions (i.e., all atomic positions and cell parameters are variable; *P*1 symmetry). Atomic positions are initialized from crystallographic data (e.g., Effenberger et al.<sup>45</sup>).

Surfaces are created by cleaving the minimized bulk structure along the (10 $\bar{1}$ 4) plane bound by the [42 $\bar{1}$ ] and [010] orthogonal vectors (2 × 10 unit cells, 7 monolayers of atoms deep, 4200 atoms). The cleavage surface is the kernel of a 3D periodic system (slab model) with crystal faces separated by 40 Å of vacuum. The surface energy  $\gamma$  (kJ m<sup>-2</sup>) is calculated as follows:

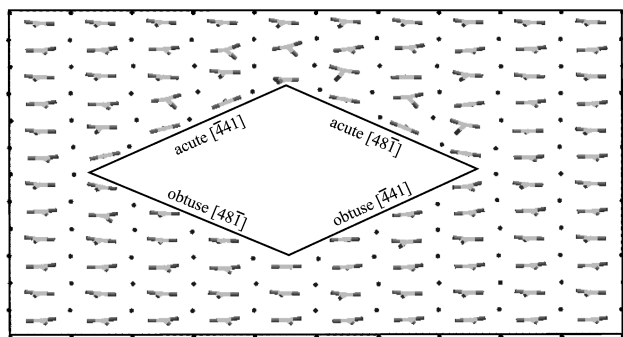
$$\gamma = \frac{U_s - U_b}{A_f} \quad (7)$$

where *U*<sub>s</sub> is the minimized energy of the system having the (10 $\bar{1}$ 4) surface (kJ mol<sup>-1</sup>), *U*<sub>b</sub> is the minimized energy of a bulk system with the same number of atoms (kJ mol<sup>-1</sup>), and *A*<sub>f</sub> is the relaxed surface area (m<sup>2</sup>) ( $\Delta A < 2\%$  for all simulations). *U*<sub>s</sub> and *U*<sub>b</sub> are calculated by eq 1 under the described system constraints (i.e., set up with a surface or as bulk). Because *U*<sub>s</sub> and *U*<sub>b</sub> are for the same number of atoms and the term is normalized by area,  $\gamma$  is independent of system size. Control simulations indicate negligible interactions of successive layers of surface across the vacuum layer, as determined by a comparison of the slab model with a system having periodicity in only two dimensions (half space).

Pits are created by removing *n* ion pairs from the first layer of a surface (*n* = 1, 2, 8, 16, or 32). Monolayer rhombohedral pits bound by [44 $\bar{1}$ ] and [48 $\bar{1}$ ] steps result (Figure 2); greater pit depths are not examined in this study. The energy per ion pair required to form a pit of *n* ion pairs on the surface is the pit formation excess energy

(44) Cygan, R. T. *Molecular modeling in mineralogy and geochemistry*. In *Molecular Modeling Theory: Applications in the Geosciences*; Cygan, R. T., Kubicki, J. D., Eds.; Mineralogical Society of America: Washington, DC, 2001; Vol. 42, p 1.

(45) Effenberger, H.; Mereiter, K.; Zemann, J. *Z. Kristallogr.* **1981**, *156*, 233.



Similar to Figure 1A in oblique view

**Figure 2.** Minimized pitted (10 $\bar{1}4$ ) calcite surface simulated using an atomistic rigid ion model. The pit depicted has 16 ion pairs removed. To emphasize the shape of the pit, only the top layer of the simulation is shown and the surface is viewed at an oblique angle. Legend: calcium, black; carbon, light gray; oxygen, dark gray.

( $\bar{\epsilon}$ ). The calculation is as follows:<sup>40</sup>

$$\Delta n \bar{\epsilon} = (U_{p,n}) - (U_{p,n-\Delta n} + \Delta n \bar{U}_b) \quad (8)$$

where  $U_{p,n}$  (kJ mol<sup>-1</sup>) is the energy of the system having an  $n$  ion pair monolayer pit,  $U_{p,n-\Delta n}$  (kJ mol<sup>-1</sup>) is the energy of the system having a monolayer pit reduced by  $\Delta n$  ion pairs, and  $\bar{U}_b$  is the energy of an ion pair in the bulk (kJ mol<sup>-1</sup> ion pair<sup>-1</sup>).

For the construction of charge-neutral pits, placement of terminating carbonate groups at either the obtuse or acute vertices of the pit is arbitrary. In a sensitivity test, we find that the energy difference between these placements is under 0.04 kJ mol<sup>-1</sup>, indicating that the carbonate is approximately equivalent for either vertex. To remain self-consistent, all further simulations have the terminating carbonate at the more stable obtuse vertex.

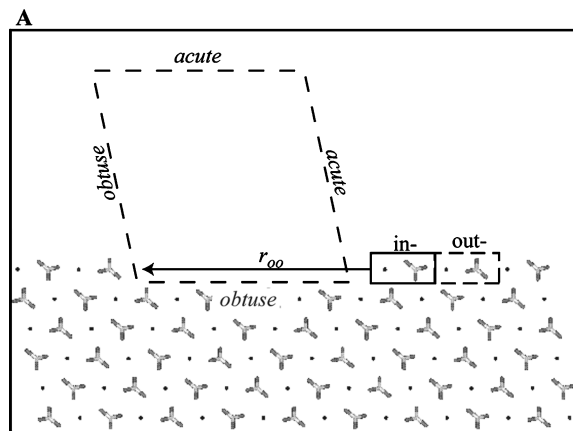
The ion pair translation energies along the obtuse and acute steps are investigated. First, a surface is created as the unrelaxed (10 $\bar{1}4$ ) plane bound by the  $[\bar{4}41]$  and  $[48\bar{1}]$  vectors (cf. Figure 1D;  $2 \times 2$  unit cells, 7 layers deep). Second, half of the atoms in the top layer of the surface are removed in a manner creating infinitely long  $[\bar{4}41]$  steps (9340 atoms). A kink ion pair of M-CO<sub>3</sub> is moved along the  $[\bar{4}41]$  step at intervals corresponding to 0.08 ion pair units (Figure 3). The energy at each position is calculated as follows:

$$\delta U_x = U_x - U_{x=0} \quad (9)$$

where  $x$  is the distance from the initial kink measured in ion pair units,  $\delta U_x$  (kJ mol<sup>-1</sup>) is the incremental translation energy when the ion pair is  $x$  units from the kink,  $U_{x=0}$  (kJ mol<sup>-1</sup>) is the system energy when the ion pair is in its initial position, and  $U_x$  (kJ mol<sup>-1</sup>) is the system energy when the ion pair is  $x$  units from the initial kink. Because calculations of  $U_x$  and  $U_{x=0}$  differ by the positioning of one ion pair,  $\delta U_x$  is independent of system size. Due to computational expense, the calculations are performed for the bulk minimum energy configuration.

### 3. Results and Discussion

This section is organized as follows: Section 3.1 presents the calculated bulk, surface, pit, and step energies. Section 3.2 tests our hypothesis of linear relationships between the calculated energies of this study and experimentally observed dissolution rates. Section 3.3 summarizes our conclusions.



Similar to Figure 1A

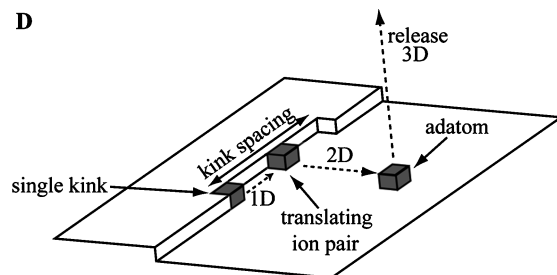
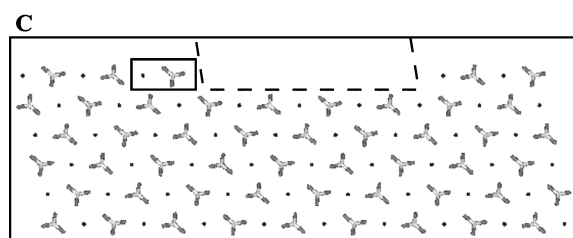
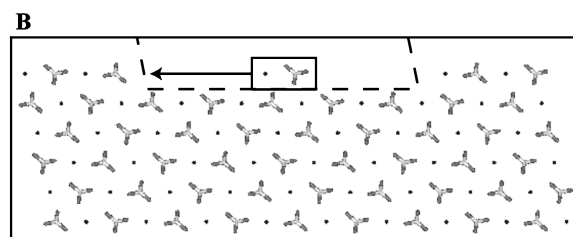


**Figure 3.** Translation pathways for an ion pair on a  $[\bar{4}41]$  calcite step viewed from above the pit. Positions shown correspond to distances of (A) 0, (B) 2, and (C) 4 formula units in Figure 5. For clarity, atoms comprising the terrace underneath the step are not shown. In panel A, the relationship between the step and the pit is shown. Examples of in-/out-oriented carbonates are also shown. (D) Generalized dissolution pathway for an ion pair released from a single-kink site. The degree of freedom for each translation is indicated by 1D (along a step), 2D (across a surface), and 3D (into aqueous solution). Figure 3 shows the energy of 1D translation. Legend: calcium, black; carbon, light gray; oxygen, dark gray.

**3.1. Energy Calculations.** We employ a rigid ion model to simulate the structural and energetic properties of carbonate minerals. Other theoretical approaches, including quantum mechanical and shell models, have a high computational cost for representing a large-sized system with surficial pits. Rigid ion models are a feasible cost-effective alternative that can accommodate the thousands of atoms represented in our carbonate simulations.

**3.1.1. Bulk Structures and Energies.** The measured and calculated physical properties (density  $\rho$ , lattice

**Table 2. Measured (Literature) and Calculated (This Study) Physical Properties of the Rhombohedral Carbonate Minerals<sup>a</sup>**

	calcite Ca	otavite Cd	sphaerocobaltite Co	siderite Fe	magnesite Mg	rhodochrosite Mn	gaspeite Ni	smithsonite Zn
Measured Physical Properties								
$\rho$ (g cm <sup>-3</sup> )	2.7106	5.024	4.208	3.937	3.010	3.72	4.35	4.434
$a$ (Å)	4.9896	4.923	4.6581	4.6916	4.6328	4.7682	4.621	4.6526
$c$ (Å)	17.0610	16.287	14.958	15.3796	15.0129	15.6354	14.93	15.0257
C–O (Å)	1.285	1.281		1.287	1.286	1.290		1.287
M–O (Å)	2.360	2.288		2.144	2.102	2.190		2.111
$\Delta H_L$ (kJ mol <sup>-1</sup> )	2811	3052	3235	3169	3122	3092		3273
Calculated Physical Properties								
$\rho$ (g cm <sup>-3</sup> )	2.784	4.939	4.186	3.863	2.951	3.657	4.298	4.412
$a$ (Å)	4.9473	4.9108	4.6486	4.7172	4.6560	4.7776	4.6119	4.6490
$c$ (Å)	16.8982	16.6531	15.1262	15.5056	15.1648	15.8429	14.9376	15.1272
C–O (Å)	1.2805	1.2809	1.2834	1.2823	1.2834	1.2820	1.2833	1.2834
M–O (Å)	2.3337	2.3054	2.1150	2.1638	2.1201	2.2068	2.0899	2.1152
$U_L$ (kJ mol <sup>-1</sup> )	2927	2933	3098	3071	3087	3013	3155	3098

<sup>a</sup> Sources of structural data: calcite, ref 45; otavite, ref 71; sphaerocobaltite, ref 72; siderite, ref 45; magnesite, ref 45; rhodochrosite, ref 45; gaspeite, ref 72; and smithsonite, ref 45. Lattice energies are provided in ref 46.

parameters  $a$  and  $c$ , bond lengths, and lattice energies) of rhombohedral carbonate minerals are shown in Table 2. Differences of the calculated versus measured structural parameters are less than 2.5%. As a point of comparison, using shell models Fiesler et al.<sup>33</sup> obtain structural differences of 1% for rhombohedral carbonate minerals, while de Leeuw<sup>35</sup> reports differences under 4% for calcite and magnesite. We conclude that the rigid ion model is equally accurate in representing the bulk carbonate structures. Furthermore, our calculated lattice energies are within 180 kJ mol<sup>-1</sup> of thermodynamic measurements.<sup>46</sup>

**3.1.2. Structures and Energies of Relaxed Terrace Surfaces.** Figure 4 shows a comparison of the unrelaxed and fully relaxed (1014) surfaces of calcite. Upon relaxation, carbonate groups rotate and oxygen atoms retract into the surface. The retraction is visible in Figure 4B. Calcium also relaxes slightly into the surface. Figure 4C shows the O–C–O bending angle ( $\theta$ ) for different layer depths. In-plane distortion of the bending angle ( $|\theta - \theta_0|$ ) is up to 39°, while there is little change of the out-of-plane dihedral O–C–O–O angle ( $|\varphi - \varphi_0| < 1^\circ$ ; CO<sub>3</sub><sup>2-</sup> remains planar). The distortion lessens with greater depth. Other members of the rhombohedral carbonate family relax with structural changes similar to those for calcite (not shown).

In contrast to this paper and another recent study,<sup>47</sup> other previous work<sup>33,41,48,49</sup> finds that carbonate groups of vacuum-terminated surfaces relax by distortion of the dihedral O–C–O–O angle. This difference arises from the modification of the intracarbonate potential parameter for the out-of-plane distortion (i.e., the dihedral four-body term): the modification improves the performance of surface models.<sup>47</sup> Our more rigid dihedral angle is consistent with spectroscopic and atomic force microscope observations indicating carbonate relaxes by rotation and in-plane distortion.<sup>50,51</sup> Despite these modifications, there is good agreement between our calculated surface energies (eq 7) and those reported previously (Table 3).

**3.1.3. Structure of Simulated Pits.** The calculated structure of a relaxed pit on calcite is shown in Figure 2

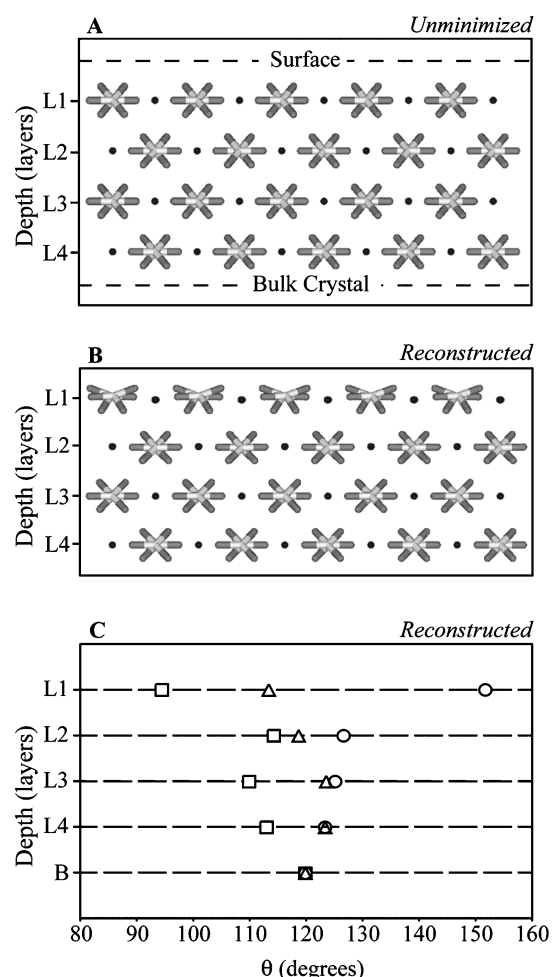


**Figure 4.** (A) Unminimized calcite surface without reconstruction. (B) Calculated reconstruction of the same surface using an atomistic rigid ion model. (C) Bending angles of carbonate for different layer depths. Markers indicate the three angles between oxygen atoms in a carbonate group. Note: The view superimposes successive carbonate ions of differing orientations, giving the false appearance of a carbonate of 6-fold coordination.

( $n = 16$ ). In addition to surface relaxation (e.g., Figure 3B), ions surrounding the pit relax by translation and molecular rotation. On the acute step, carbonates rotate and orient with the step. Carbonates also rotate away from the pit, opening the angle between the step and the

(46) *CRC Handbook of Chemistry and Physics*; Lide, D. R., Ed.; CRC Press: Boca Raton, FL, 2000; Vol. 81.

(47) Rohl, A. L.; Wright, K.; Gale, J. D. *Am. Mineral.* **2003**, *88*, 921.

(48) Catti, M.; Pavese, A.; Price, G. D. *Phys. Chem. Miner.* **1993**, *19*, 472.

(49) Pavese, A.; Catti, M.; Price, G. D.; Jackson, R. A. *Phys. Chem. Miner.* **1992**, *19*, 80.

(50) Fenter, P.; Geissbuhler, P.; DiMasi, E.; Srajer, G.; Sorensen, L. B.; Sturchio, N. C. *Geochim. Cosmochim. Acta* **2000**, *64*, 1221.

(51) Liang, Y.; Lea, A. S.; Baer, D. R.; Engelhard, M. H. *Surf. Sci.* **1996**, *351*, 172.

**Table 3. Calculated Surface Energies under Vacuum ( $\text{J m}^{-2}$ )**

cation	this study	Wright et al. (ref 42)	DeLeeuw (ref 35)	Hwang et al. (ref 43)
Ca	0.404	0.322	0.59	0.86
Cd	0.408			
Co	0.485			
Fe	0.471			
Mg	0.478	0.232	0.76	
Mn	0.442			
Ni	0.481			
Zn	0.536			

pit floor (e.g., Figure 6C,D). Distortion also occurs for the second row of ions bordering the step. Analogous simulations for pits ranging in size from 1 to 32 ion pairs yield qualitatively similar results, as do simulations for all eight rhombohedral carbonate compositions.

**3.1.4. Ion Pair Translation Energies.** The process of an ion pair moving along the obtuse [441] step is depicted in Figure 3A–C for calcite. In Figure 3A, the ion pair is at its initial single-kink position ( $x = 0$ ). In Figure 3B, the ion pair translates to a site two ion pair lengths away ( $x = 2$ , 12.725 Å translation). In Figure 3C, the ion pair fully translates to the other side of the step, where it is now at a kink site equivalent to its original position but four ion pair lengths away ( $x = 4$ , 25.550 Å).

The energy change  $\delta U_x$  for the Ca–CO<sub>3</sub> ion pair at different positions accompanying translation is shown for an obtuse step in Figure 5A and an acute step in Figure 5B. There are two energy profiles, which correspond to the in- and out- orientations of the carbonates at differing initial positions. For example, an in- carbonate moving in direction  $r_{oo}$  (cf. Figure 1D) is shown in Figure 3A. In a return trip, this in- carbonate moves in direction  $r_{oa}$ . Although ion pair movement along the obtuse step is nearly independent of in-/out- orientation, on the acute step the two orientations have differing energy profiles. An additional interesting feature of Figure 5 is that the first energy barrier encountered by an ion pair on moving in the direction  $r_{oo}$  on the obtuse step is significantly less than for the movement in the direction  $r_{oa}$ , whereas an ion pair moving in the direction  $r_{aa}$  on the acute step faces an initial energy barrier similar to that of movement in the direction  $r_{ao}$ .

The differing behavior for in-/out- translation along obtuse versus acute steps is rationalized by structure. For both steps, the energy minima occur at positions like  $x = 2$  where the oxygens of the translating ion pair have the greatest distances from oxygens in the step and the underlying terrace (viz., 3.159 Å). The energy maxima occur at positions such as  $x = 1.5$  where oxygens of the translating ion pairs are at their smallest distances from lattice oxygens. Along the acute step, the exact distances and energies depend on the in-/out- orientation; however, there is no dependency along the obtuse step (Figures 5B and 6C,D versus Figures 5A and 6A,B). The energy differences along the acute step arise not from the closest intercarbonate O–O distance, which is 1.525 Å for both in- and out- carbonates, but rather from the second closest intercarbonate O–O distance, which is 2.087 Å for out-compared to 1.932 Å for in- carbonates of calcite (Figure 6C,D). Similar geometric relationships between energy and atomic distance exist for the other members of the rhombohedral carbonate family.

The absolute magnitudes of the energy maxima shown in Figure 5 are not realistic for chemical processes. The high values arise because these surface systems are artificially constructed and are not allowed to relax to their lowest energy configurations. As a result, the

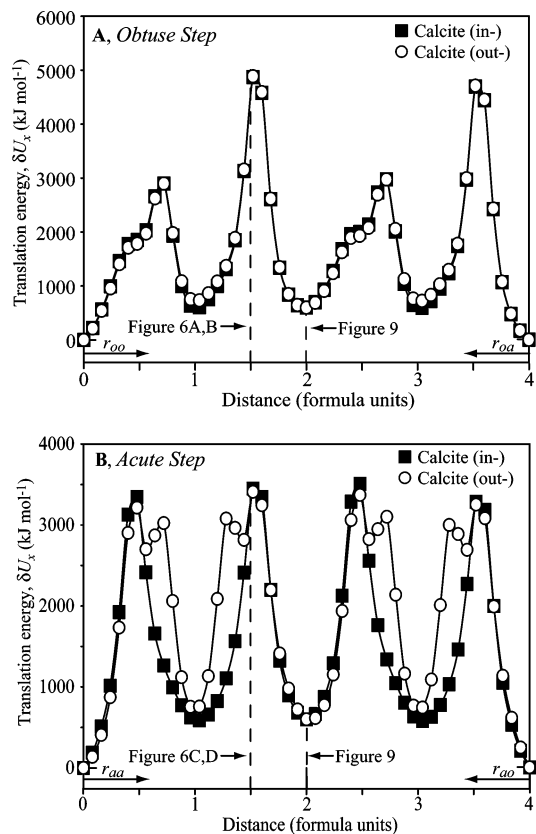


**Figure 5.** Translation energy of an ion pair on a calcite [441] step. (A) Obtuse step. (B) Acute step. Dashed lines show the positions depicted in Figures 6 and 9.

translated ion pairs assume highly energetically unfavorable configurations that would not occur in real systems. For example, at an energy maximum, an oxygen atom of the translated carbonate is only 1.525 Å from an oxygen atom in a step carbonate, and large repulsive interactions result. Although the absolute energies reported in Figure 5 do not reflect realistic ion pair translation energies, they are nevertheless useful for relative comparisons among minerals.

**3.2. Linear Relationships between Energies and Dissolution Rates.** A major goal of our work is to test for correlations between calculated energies and measured dissolution rates. Calculated quantities include lattice energy ( $\text{kJ mol}^{-1}$ ), surface energy ( $\text{J m}^{-2}$ ), pit formation excess energy ( $\text{kJ mol}^{-1}$  ion pair<sup>-1</sup>), and translation energy of an ion pair along a step ( $\text{kJ mol}^{-1}$ ). Measured dissolution rates include the macroscopic rate of material removal ( $\text{mol m}^{-2} \text{s}^{-1}$ ) and the microscopic step retreat velocity ( $\text{nm s}^{-1}$ ). The microscopic step retreat velocity can be scaled geometrically to macroscopic dissolution rates with knowledge of the step density, step height, and molar volume.<sup>25,52–56</sup> In extrathermodynamic relationships, the kinetic parameters correlate with Gibbs free energy ( $\Delta G$ ) as LFERs. Correlations occur when the transition state energy ( $\Delta G^\ddagger$ ) is proportional to the free energy of the reaction.<sup>57,58</sup> To relate our calculated energies to dissolution rates, we assume that our calculated energy is the

(52) Jordan, G.; Rammensee, W. *Geochim. Cosmochim. Acta* **1998**, *62*, 941.

(53) Shiraki, R.; Rock, P. A.; Casey, W. H. *Aquat. Geochem.* **2000**, *6*, 87.

(54) Higgins, S. R.; Jordan, G.; Eggleston, C. M. *Geochim. Cosmochim. Acta* **2002**, *66*, 3201.

(55) Dove, P. M.; Platt, F. M. *Chem. Geol.* **1996**, *127*, 331.

(56) MacInnis, I. N.; Brantley, S. L. *Geochim. Cosmochim. Acta* **1992**, *56*, 1113.

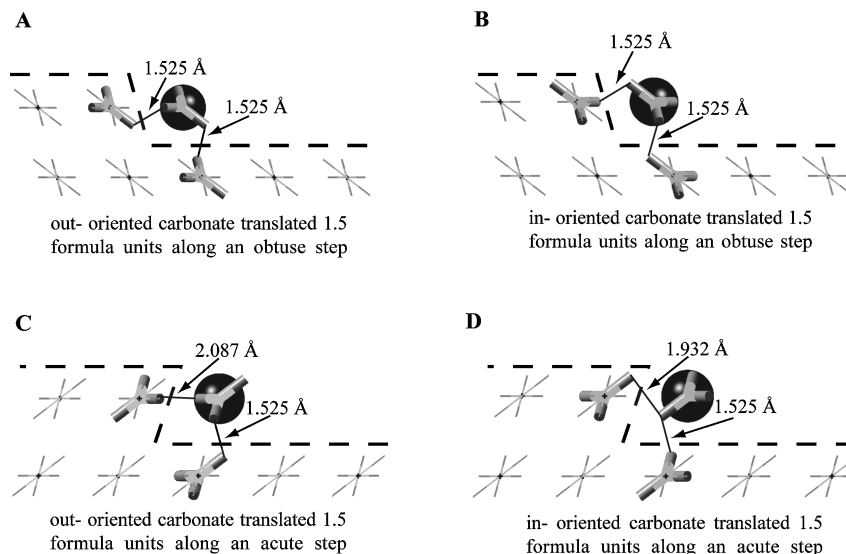


**Figure 6.** Ion pair at a maximum energy position ( $x = 1.5$ , Figure 5) on a  $[441]$  calcite step viewed from the side. The viewpoint in Figure 6 is shown as the asterisk in Figure 1A. Translation in Figures 3 and 5 occurs at a monolayer step oriented in-and-out of the page at the asterisk in Figure 1A. The crystal face defined by the atomic scale orientation of obtuse step is  $(3\bar{1}216)$ , while the acute step is  $(3148)$  (ref 40). (A) Out- carbonate on an obtuse step. (B) In- carbonate on an obtuse step. (C) Out- carbonate on an acute step. (D) In- carbonate on an acute step. The translating ion pair contacts carbonates both in the step and in the terrace of the pit bottom. Because  $x$  denotes the relative distance from the initial corner position of the ion pair and because the corner position depends on in- versus out- orientation (Figure 3A), the orientations of carbonate ions in the step and in the terrace closest to the translated ion pair are different for in- and out- carbonates (cf. panels A and B). Legend: calcium, black; carbon, light gray; oxygen, dark gray.

dominant contributor to the free energy (i.e., the entropic contribution is negligible).

**3.2.1. Similarities between Vacuum-Terminated and Circumneutral Aqueous Surfaces.** There are similarities between our simulated vacuum-terminated surfaces and surfaces exposed to aqueous circumneutral conditions. The surface is composed of two amphoteric sites, including a carbonate group ( $>CO_3H$ ) and a metal hydroxyl group ( $>MOH$ ).<sup>59–61</sup> At circumneutral pH, the dominant surface speciation is predicted as a deprotonated  $>CO_3^-$  group and a twice protonated  $>MOH_2^+$  group, as confirmed by recent spectroscopic measurements of calcite and dolomite.<sup>50,62</sup> The surface charge is approximately neutral. Furthermore, the hydroxide moieties are positive with the carbonates correspondingly negative; that is, total charge separation occurs. We conclude that surfaces under these circumneutral aqueous conditions lack complex protonation and in more than one aspect are similar to surfaces in our energy calculations.

**3.2.2. Bulk Energies and Dissolution Rates.** The lattice energies calculated by eq 1 predict the measured macroscopic dissolution rates (Figure 7), for both powder and single-crystal dissolution rates. An explanation is that a large lattice energy indicates a stable ionic structure, which can be expected to dissolve slowly relative to those crystal structures having smaller lattice energies. The effects of ion solvation and surface hydration are not treated in our calculations due to computational expense.

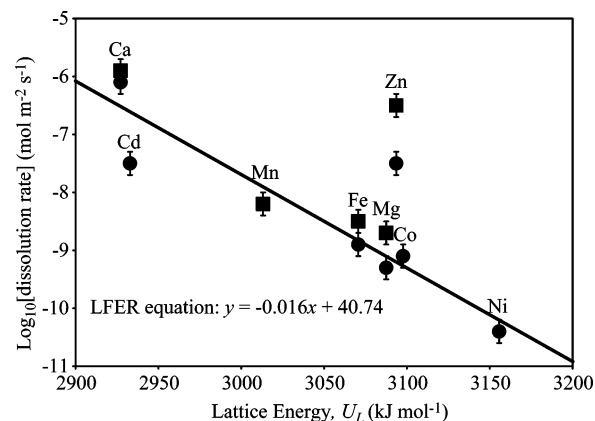


**Figure 7.** Linear free energy relationship (LFER) between the log of the circumneutral dissolution rate and the calculated lattice energy. Squares: dissolution of the  $(10\bar{1}4)$  crystal face. Circles: powder dissolution rates. Sources of single-crystal macroscopic dissolution rates: calcite, ref 30; siderite, ref 24; magnesite, ref 23; rhodochrosite, ref 25; and smithsonite, ref 23. Powder dissolution rates are from ref 60.

Presumably, the inclusion of this term in the free energies would improve the accuracy of the correlations. However, the success of this correlation suggests that the dominant difference in reaction energies arises from the lattice energy, at least for this isostructural series of minerals.

Smithsonite ( $ZnCO_3$ ) is an outlier in the correlation of calculated energies with dissolution rates. Unlike other carbonates, smithsonite does not dissolve via the formation of rhombohedral pits. Instead, triangular or other distorted pits and furrows form.<sup>23</sup> These observations suggest a different dissolution mechanism for  $ZnCO_3$ . Of further note, Elzinga and Reeder<sup>11</sup> report that zinc forms tetrahedral adsorption complexes on calcite, unlike other  $M^{2+}$  ions in the rhombohedral carbonate family, which favor octahedral coordination. We postulate that  $Zn^{2+}$  adsorbed to the  $ZnCO_3$  surface is in tetrahedral coordination.

(57) Brezonik, P. L. Principle of linear free-energy and structure–activity relations and their application to the fate of chemicals in aquatic systems. In *Aquatic Chemical Kinetics*; Stumm, W., Ed.; Wiley: New York, 1990; p 113.

(58) Lasaga, A. C. *Kinetic Theory in the Earth Sciences*; Princeton University Press: Princeton, 1998.

(59) Van Cappellen, P.; Charlet, L.; Stumm, W.; Wersin, P. *Geochim. Cosmochim. Acta* **1993**, *57*, 3505.

(60) Pokrovsky, O. S.; Schott, J. *Environ. Sci. Technol.* **2002**, *36*, 426.

(61) Pokrovsky, O. S.; Schott, J.; Thomas, F. *Geochim. Cosmochim. Acta* **1999**, *63*, 863.

(62) Pokrovsky, O. S.; Mielczarski, J.; Barres, O.; Schott, J. *Langmuir* **2000**, *16*, 2677.

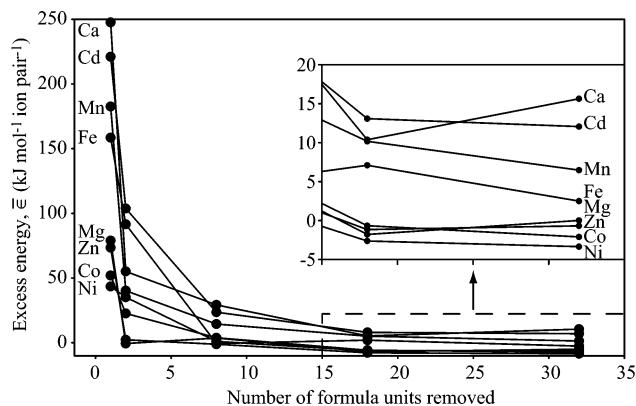


**Figure 8.** The dependence of pit formation partial excess energy on pit size. Solid lines are to guide the eye and do not represent a model fit. The inset shows the boxed region of the figure in greater detail.

**3.2.3. Excess Energies during the Initial Stages of Pit Formation.** The expansion of microscale pits is readily observable by optical interferometry<sup>56,63</sup> and scanning probe microscopy (e.g., Figure 1). However, direct observation of the initial angstrom-scale genesis has not been experimentally accomplished to date. To study the energetics of pit formation, we simulate a series of angstrom-scale monolayer pits varying in size from 1 to 32 ion pairs removed.

The dependence of the pit formation partial excess energies (eq 8) on size is shown in Figure 8. For all endmember carbonates, the excess energies asymptotically approach limiting values of  $-3$  to  $+20$   $\text{kJ mol}^{-1}$  as pit size grows. For  $n \geq 18$  ion pairs,  $\bar{\epsilon}$  is approximately constant. The rapid decrease with increasing  $n$  implies that step velocities increase during the initial stages of pit growth and reach a constant value for larger pits.<sup>64</sup>

**3.2.4. Ion Pair Translation Energies and Step Velocities.** Direct experimental observation of the dynamic elements of step retreat is not presently feasible. Nevertheless, we can apply our atomistic model within the framework of terrace–ledge–kink (TLK) theory to gain insight between crystal energetics and step retreat rates. According to TLK theory, step retreat is initiated when a single unit (e.g., an  $\text{M-CO}_3$  ion pair) dissolves from a step,<sup>53</sup> leaving behind a double-kink site.<sup>22,25,26,64,65</sup> Ion pairs progressively detach from each side of the kink (Figure 3D). The kink spacing is lengthened, each corner being a single kink. The single kinks propagate until reaching the end of the step or alternately colliding with another single kink originated from an independently formed double kink on the same step. A further complication, caused by the anisotropic nature of rhombohedral carbonates, is that four distinct rates of single-kink propagation exist:  $r_{oo}$ , which is the propagation rate ( $\text{m s}^{-1}$ ) of a single kink on an obtuse step moving toward an obtuse step;  $r_{oa}$ , on an obtuse step moving toward an acute step;  $r_{ao}$ , on an acute step moving toward an obtuse step; and  $r_{aa}$ , on an acute step moving toward an acute step (e.g., Figures 1D and 3). Dissolution therefore occurs anisotropically at the microscale. Obtuse steps retreat more rapidly than acute steps under most investigated experimental conditions.<sup>25,52,66,67</sup>

(63) Lutge, A.; Winkler, U.; Lasaga, A. C. *Geochim. Cosmochim. Acta* **2003**, *67*, 1099.

(64) McCoy, J. M.; LaFemina, J. P. *Surf. Sci.* **1997**, *373*, 288.

(65) Liang, Y.; Baer, D. R.; McCoy, J. M.; LaFemina, J. P. *J. Vac. Sci. Technol., A* **1996**, *14*, 1368.

(66) Liang, Y.; Baer, D. R. *Surf. Sci.* **1997**, *373*, 275.

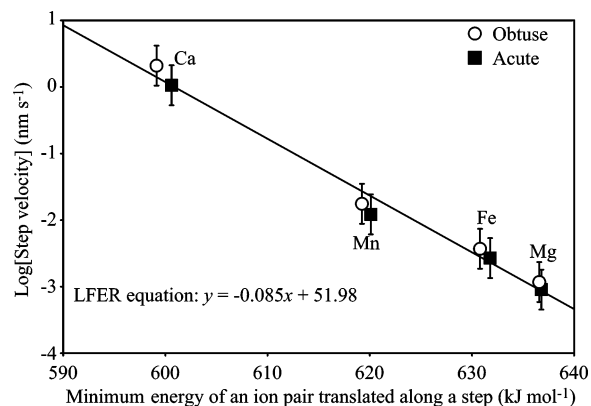


**Figure 9.** Log-linear relationship between step velocity and the minimum energy of an ion pair translated along a step (viz.  $x = 2$  in Figure 5). Sources of microscopic step retreat rates: calcite, ref 30; siderite, ref 23; magnesite, ref 23; and rhodochrosite, ref 25.

We hypothesize that the rate-determining process in step retreat is tied to the sequential breaking of the ionic bonds during single-kink propagation. A calcite ion pair at a kink site has three bonds to the surface. To dissolve, it must sequentially (a) break one bond, (b) translate along the step to a metastable position having two bonds, (c) break one bond, (d) diffuse across the surface by a one-bond tether, and (e) break the final bond, leading to dissolution into solution (Figure 3D).<sup>58,68–70</sup> To examine process c as the rate-determining process, we calculate the translation energy of an ion pair along a step (Figure 5).

The most stable position of an ion pair on a step is at  $x = 2$ . We assume that this site is the long-lived reaction intermediate of process (b) from which detachment of the ion pair occurs. We further assume that the energy of the ion pair in this position is a surrogate energy of the entire ion pair detachment. This energy will then predict step velocity. The correlation is shown in Figure 9 for both the acute and obtuse steps. Our second assumption is rationalized by noting that ion pair detachment is composed of the sequential breaking of similar ionic bonds (e.g.,  $\text{M-O}$ ), which suggests that the energy of each individual bond cleavage correlates with the overall energy of the entire ion pair detachment.

**3.3. Conclusions.** A rigid ion model successfully predicts the structural and energetic properties of rhombohedral carbonate minerals. A log-linear relationship between calculated lattice energies and measured macroscopic dissolution rates is established. The implication is that high bond strength leads to slow dissolution rates, although this result may only hold for a series of isostructural minerals that dissolve by the same mechanism.

The rigid ion model is further applied to simulate the microscopic processes active in dissolution. In early stages of pit formation, step velocities are predicted to increase

(67) Teng, H. H.; Dove, P. M.; Orme, C. A.; De Yoreo, J. J. *Science* **1998**, *282*, 724.

(68) Morse, J. W.; Arvidson, R. S. *Earth Sci. Rev.* **2002**, *58*, 51.

(69) Zhang, J. W.; Nancollas, G. H. Mechanisms of growth and dissolution of sparingly soluble salts. In *Mineral–Water Interface Geochemistry*; Hochella, M. F., Jr., White, A. F., Eds.; American Mineralogical Society: Washington, DC, 1990; Vol. 23, p 365.

(70) Macpherson, J. V.; Unwin, P. R. *Prog. React. Kinet.* **1995**, *20*, 185.

(71) Borodin, V. L.; Lyutin, V. V.; Iliukhin, V. V.; Belov, N. V. *Dokl. Akad. Nauk SSSR* **1979**, *245*, 1099.

(72) Gaines, R. V.; Skinner, H. C. W.; Foord, E. E.; Mason, B.; Rosenzweig, A. *Dana's New Mineralogy*, 8th ed.; Wiley: New York, 1997.

with growing size. For larger pits, we show that ion pair translation energies predict experimentally observed step velocities. When applied in conjunction with experimental observations, molecular modeling is an especially valuable tool for understanding the atomic energies and mechanisms of surface reactions.

**Acknowledgment.** O.W.D. is the recipient of a Sandia National Laboratories Campus Executive Fellowship. S.T.M. is grateful for support received from the New York Community Trust Merck Fund and from the Chemical

Sciences, Geosciences, and Biosciences Division of the Office of Basic Energy Sciences in the U.S. Department of Energy. R.T.C. acknowledges the support provided by the Chemical Sciences, Geosciences, and Biosciences Division of the Office of Basic Energy Sciences in the U.S. Department of Energy. Sandia is a multiprogram laboratory operated by Sandia Corporation, a Lockheed Martin company, for the United States Department of Energy under Contract DE-AC04-94AL85000.

LA035348X